

# Chiral Recognition: A Spin-Driven Process in Chiral Oligothiophene. A Chiral-Induced Spin Selectivity (CISS) Effect Manifestation

Andrea Stefani, Tommaso Salzillo, Patrizia Romana Mussini, Tiziana Benincori, Massimo Innocenti, Luca Pasquali, Andrew C. Jones, Suryakant Mishra, and Claudio Fontanesi\*

In this paper it is experimentally demonstrated that the electron-spin/molecular-handedness interaction plays a fundamental role in the chiral recognition process. This conclusion is inferred comparing current versus potential ( $I-V$ ) curves recorded using chiral electrode surfaces, which are obtained via chemisorption of an enantiopure thiophene derivative: 3,3'-bibenzothiophene core functionalized with 2,2'-bithiophene wings ( $BT_2T_4$ ). The chiral recognition capability of these chiral-electrodes is probed via cyclic voltammetry measurements, where, Ag nanoparticles (AgNPs) capped with enantiopure  $BT_2T_4$  ( $BT_2T_4@AgNP$ ) are used as the chiral redox probe. Then, the interface handedness is explored by recording spin-polarized  $I-V$  curves in spin-dependent electrochemistry (SDE) and magnetic-conductive atomic force microscopy (mc-AFM) experiments. The quality of the interfaces is thoroughly cross-checked using X-ray photoemission spectroscopy, Raman, electrodesorption measurements, which further substantiate the metal(electrode)-sulfur(thiophene) central role in the chemisorption process. Spin-polarization values of about 15% and 30% are obtained in the case of SDE and mc-AFM experiments, respectively.

## 1. Introduction

Chirality is an exceptionally transversal and interdisciplinary field of science, profoundly connected to biology, chemistry, physics, and mathematics. As a concept, chirality is often conveyed in terms of the left and right hands specular images, which is by far an oversimplified picture of a much more complex subject. For instance a distinction must be made between “true” and “false” chirality.<sup>[1]</sup> Furthermore, properties deeply related with the concept of handedness, and apparently unrelated to “chirality,” are 1) magnetism, where polar and axial vectors play a central role<sup>[2]</sup> 2) spin 3) the photon helicity.<sup>[3–5]</sup> In biology chirality is of primary importance, proteins and DNA are chiral, and in addition, biorelated molecular architectures are present in nature with a single handedness, this evidence is addressed as the

A. Stefani  
Department of Physics  
Informatics and Mathematics ‘FIM’  
University of Modena and Reggio Emilia  
Via Giuseppe Campi, 213, Modena 41125, Italy  
A. Stefani, L. Pasquali, C. Fontanesi  
Department of Engineering ‘Enzo Ferrari’  
DIEF  
University of Modena and Reggio Emilia  
Via Vivarelli 10, Modena 41125, Italy  
E-mail: claudio.fontanesi@unimore.it

T. Salzillo  
Department of Industrial Chemistry “Toso Montanari”  
University of Bologna  
Viale del Risorgimento, 4, Bologna 40136, Italy  
P. R. Mussini  
Department of Chemistry  
University of Milano  
Via Golgi 19, Milano 20133, Italy  
T. Benincori  
Department of Science and Technology  
DISAT  
University of Insubria  
Via Valleggio 11, Como 22100, Italy  
M. Innocenti  
Department of Chemistry  
“Ugo Schiff”  
Univ. of Firenze  
via della Lastruccia 3, Sesto Fiorentino 50019, Italy

 The ORCID identification number(s) for the author(s) of this article can be found under <https://doi.org/10.1002/adfm.202308948>

© 2023 The Authors. Advanced Functional Materials published by Wiley-VCH GmbH. This is an open access article under the terms of the Creative Commons Attribution-NonCommercial-NoDerivs License, which permits use and distribution in any medium, provided the original work is properly cited, the use is non-commercial and no modifications or adaptations are made.

DOI: 10.1002/adfm.202308948

“homochirality problem,” a yet to be solved fundamental conundrum.<sup>[6]</sup> Within this picture, chiral recognition and enantioselectivity rule asymmetric processes from chemical synthesis to biological life cycles. Enantio-recognition can be probed by circular dichroism (CD) spectroscopies,<sup>[7]</sup> electrochemically,<sup>[8]</sup> analytical separation in chromatography.<sup>[9]</sup> Applicative aspects concern sensors<sup>[10–12]</sup> resolution of racemic mixtures<sup>[13–16]</sup> drug synthesis and chemical reactivity,<sup>[17–19]</sup> chiral induction,<sup>[20,21]</sup> and light-driven molecular motors.<sup>[22]</sup> Chiral recognition was assumed to be controlled by geometrical-based interactions, the “lock and key” and “Three-Point Interaction” models, but chiral recognition is recognized as still lacking a physical-based detailed explanation.<sup>[23]</sup> Recently, spin-based exchange interactions have been proposed to rule chiral-induction, i.e., the ability of a chiral compound to induce chirality in an achiral system.<sup>[24]</sup> Indeed, the physics underlying the emerging of specific interactions between chiral systems and spin polarized electrons is a true “hot-topic,” the magneto-chiral dichroism and CISS effects are two manifestations.<sup>[18,25–28]</sup> Remarkably, state-of-the-art diamagnetic materials characterized by good spin-polarization characteristics have been developed within this field of research.<sup>[4,29,30]</sup> Moreover, charge transmission appears unexpectedly efficient in the case of chiral systems,<sup>[31–38]</sup> and what is more, it is shown to be spin-selective,<sup>[39]</sup> and theoretical results suggest that a fundamental role is played by spin-orbit coupling (SOC).<sup>[40,39,41]</sup> In this arena, the purpose of this paper is to assess the physics of the driving force underlying chiral recognition, to this end the charge transmission of suitable chiral, metal-substrate|chemisorbed-BT<sub>2</sub>T<sub>4</sub> (hybrid), interfaces is probed by means of electrochemical and magneto contact-conductive probe (mc-AFM) measurements. Surface chirality is imparted by BT<sub>2</sub>T<sub>4</sub> self-assembled monolayers (SAM), formed exploiting the strong chemisorption of the thiophene moiety on Au, Ag, and Ni. Then, chiral recognition is probed via the implementation of three different experimental configurations, as summarized in **Figure 1B–D**. These three experiments are conceived to probe independently the interplay between chirality, molecular handedness, and spin selectivity. Experiment I: a current is transmitted through a “sandwich” of two molecular layers on gold, either of the same (symmetric) or opposed

(dissymmetric) handedness, electric contact is provided via grafted AgNPs. Experiment II: in a typical SDE setup,<sup>[42,43]</sup> a spin-polarized current is measured through molecular layers of different helicities, yet AgNPs are used as terminal contact. Experiment III: the current through an AFM magnetized tip is measured. Note that, handedness in these experiments relies on the use of two enantiopure stereoisomers of the same chemical species (R- and S- BT<sub>2</sub>T<sub>4</sub>), thus variations observed in *I*–*V* curves are exclusively due to handedness discrimination, i.e., chiral recognition.

## 2. Results and Discussion

### 2.1. Probing Molecular Handedness: Chiral Recognition

#### 2.1.1. Experiment I: Chiral Recognition

Cyclic voltammetry (CV) curves are recorded for the four possible combinations Au|(S)-BT<sub>2</sub>T<sub>4</sub>|(R)-BT<sub>2</sub>T<sub>4</sub>@AgNP, Au|(S)-BT<sub>2</sub>T<sub>4</sub>|(S)-BT<sub>2</sub>T<sub>4</sub>@AgNP, Au|(R)-BT<sub>2</sub>T<sub>4</sub>|(R)-BT<sub>2</sub>T<sub>4</sub>@AgNP and Au|(R)-BT<sub>2</sub>T<sub>4</sub>|(S)-BT<sub>2</sub>T<sub>4</sub>@AgNP, interfaces, i.e., probing the charge transmission of interfaces of symmetric versus dissymmetric handedness, a typical way to investigate chiral recognition.<sup>[8,44]</sup> **Figure 2A** shows the relevant actual experimental implementation.

Remarkably, the peak current (at –0.1 and 0.05 V) is larger for the “symmetric” combination, i.e., when the two facing interfaces feature the same handedness. Red curve in **Figure 2B** (S)-BT<sub>2</sub>T<sub>4</sub>|(S)-BT<sub>2</sub>T<sub>4</sub>, while the black curve in **Figure 2C** has the largest current corresponding to the (R)-BT<sub>2</sub>T<sub>4</sub>|(R)-BT<sub>2</sub>T<sub>4</sub> combination. Details concerning AgNPs preparation (and capping) and the chemisorption on Au are reported in the Supporting Information: chiral capped AgNPs synthesis (**Figures S1–S3**, Supporting Information). While, details concerning the preparation and characterization of the Au|BT<sub>2</sub>T<sub>4</sub>|BT<sub>2</sub>T<sub>4</sub>@AgNP interfaces are reported in **Sections S1.3.1** and **S1.3.2**, **Figures S4** and **S5** (Supporting Information). **Section 2** gives full details concerning gold functionalization. **Figure S6** (Supporting Information) shows X-ray photoemission spectroscopy (XPS) data, while **Figure S7** (Supporting Information) shows replicas of CVs concerning the electrochemical based chiral recognition. The effective BT<sub>2</sub>T<sub>4</sub> chemisorption on Au was further characterized by recording Raman spectra (exploiting SERS effect). Experimental Raman results are discussed in detailed based on theoretical calculations (high quality DFT B3LYP/cc-pVTZ level of the theory for the isolated BT<sub>2</sub>T<sub>4</sub> molecule, semiempirical for a cluster of BT<sub>2</sub>T<sub>4</sub> on gold) **Section 3**, **Figures S8–S11** (Supporting Information).

#### 2.1.2. Experiment II: Spin-Dependent Electrochemistry

The charge transmission through the enantiopure Ni|(S)-BT<sub>2</sub>T<sub>4</sub>@AgNPs and Ni|(R)-BT<sub>2</sub>T<sub>4</sub>@AgNPs interfaces is probed by recording CV curves (SDE) as a function of spin-injection, i.e., by application of a magnetic field UP versus magnetic field DOWN orientation (a permanent magnet is placed just under the working electrode (WE) surface, 0.5 mm away from the actual contact between the solution and ferromagnetic WE surface).

M. Innocenti, C. Fontanesi  
National Interuniversity Consortium of Materials Science and Technology (INSTM)  
Via G. Giusti 9, Firenze FI 50121, Italy  
L. Pasquali  
IOM-CNR  
Strada Statale 14, Km. 163.5 in AREA Science Park, Basovizza Trieste 34149, Italy  
L. Pasquali  
Department of Physics  
University of Johannesburg  
P.O. Box 524, Auckland Park 2006, South Africa  
A. C. Jones, S. Mishra  
Center for Integrated Nanotechnologies  
Los Alamos National Laboratory  
Los Alamos, NM 87545, USA  
S. Mishra  
Pritzker School of Molecular Engineering at University of Chicago  
5640 S Ellis Ave, Chicago, Illinois 60637, USA

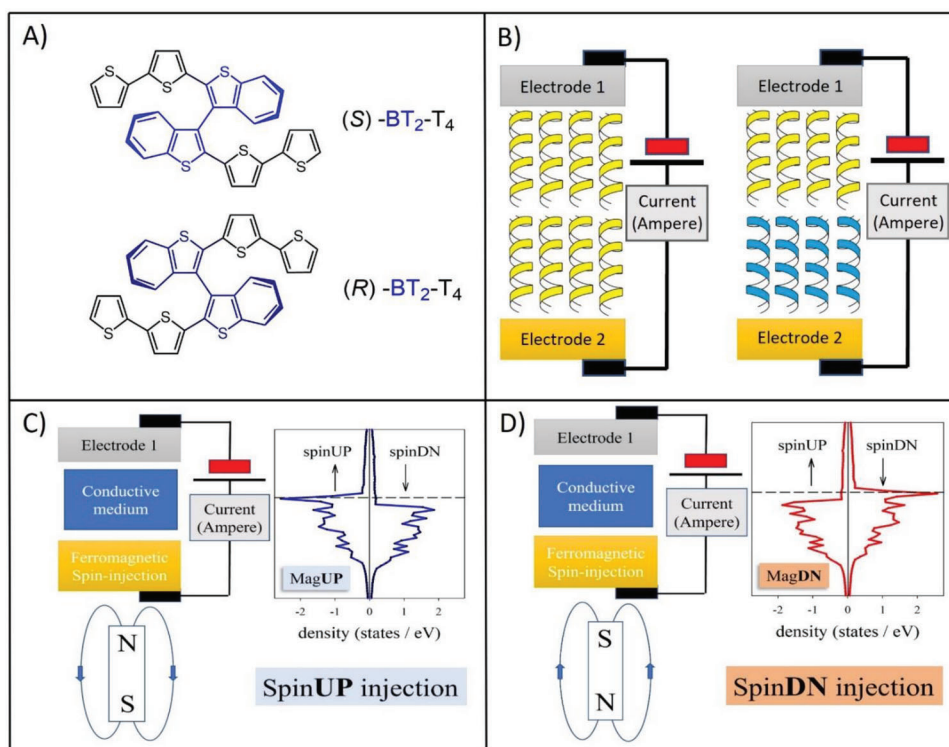


**Figure 1.** A)  $\text{BT}_2\text{T}_4$  molecular structure both the (S)- and (R) enantiomers are shown. B) Experimental setup for the “true” chiral recognition experiment: two  $\text{BT}_2\text{T}_4$  self-assembled monolayers (SAMs) are placed in tight contact with the two possible handedness combinations. Left same handedness (symmetric interface). Right the two SAMs feature opposite handedness (dissymmetric interface). C,D) Spin-injecting/spin-probing device. The energy versus density of state (DOS) pattern of the ferromagnetic electrode is shown as a function of the magnetic field orientation, the horizontal black dotted line is the Fermi energy. Blue curves DOS for magnetic field up. Red curves DOS for magnetic field down.<sup>[42]</sup>

Figure 1C,D represents schematically the physics underlying Experiment II, while **Figure 3A** shows the actual experimental implementation, the relevant experimental CV curves are presented in **Figure 3B,C**.

Remarkably, the  $I$  versus  $E$  pattern is found to be a function of the magnet orientation. What is more, for the  $\text{Ni}|\text{(S)-BT}_2\text{T}_4@\text{AgNP}$  interface the largest current peaks (at about 0.1 and  $-0.075$  V) in the CV are found for spin-injection corresponding to magnet DOWN orientation (**Figure 3B**, red curve). The opposite result (the largest current is relevant to the magnet UP orientation) is found for the  $\text{Ni}|\text{(R)-BT}_2\text{T}_4@\text{AgNP}$  interface (**Figure 3C**, black curve). Comparison of differences in current peak values **Figure 3C,D** as a function of magnet orientation allow to determine a spin polarization (SP%) value ranging between 13% and 15%. Spin polarization is defined as:

$$\text{SP}\% = \frac{(I_{\text{MagUP}} - I_{\text{MagDOWN}})}{(I_{\text{MagUP}} + I_{\text{MagDOWN}})} \times 100 \quad (1)$$

Where:  $I_{\text{MagUP}}$  and  $I_{\text{MagDOWN}}$  are the peak current values recorded with the magnet orientation UP and DOWN, respectively. The quantitative assessment of the spin-chirality interaction energy can be addressed, by considering the potential difference in between the current peaks in the CVs shown in **Figure 3B,C**, the potential shift is ranging between 50 and 100 mV. The Nernst equation  $\Delta\mu = -nFE$  ( $\Delta\mu$  is the Gibbs energy involved in the

spin-chirality interaction process,  $n$  is considered one transferred electron,  $F$  is the Faraday, and  $E$  in our case the peak potential shift due to magnet orientation) allows for a crude estimation of 5 to 10  $\text{kJ mol}^{-1}$  as the range of spin-“molecular-handedness” interaction energy. Details concerning the  $\text{BT}_2\text{T}_4$  chemisorption on Ni, and relevant characterization, are reported in the Supporting Information. Section S3.4 (Supporting Information) reports and discusses Raman spectra collected “in situ”/“in operando,” **Figure S12** (Supporting Information). Section 4.1 (Supporting Information) reports the experimental XPS spectra (**Figure S13**, Supporting Information), and relevant discussion concerning the  $\text{Ni}|\text{BT}_2\text{T}_4$  interface. Fabrication procedure and XPS characterization of the hybrid  $\text{Ni}|\text{BT}_2\text{T}_4@\text{AgNP}$  interface is presented in Section S4.2 and **Figure S14** (Supporting Information).

### 2.1.3. Experiment III: Magnetic Conductive Probe AFM

The charge transmission through the enantiopure  $\text{Au}|\text{(S)-BT}_2\text{T}_4$  and  $\text{Au}|\text{(R)-BT}_2\text{T}_4$  interfaces is determined by recording  $I$ - $V$  curves as a function of spin-injection (i.e., magnetic field UP versus magnetic field DOWN). **Figure 1C,D** represent the physics underlying Experiment III (it is the same of the Experiment II). **Figure 4A** shows the experimental setup. The relevant  $I$ - $V$  curves are presented in **Figure 4B,C**, which are recorded using a mc-AFM. In this experiment the current between the AFM tip and the surface is recorded as a function of the magnetic field

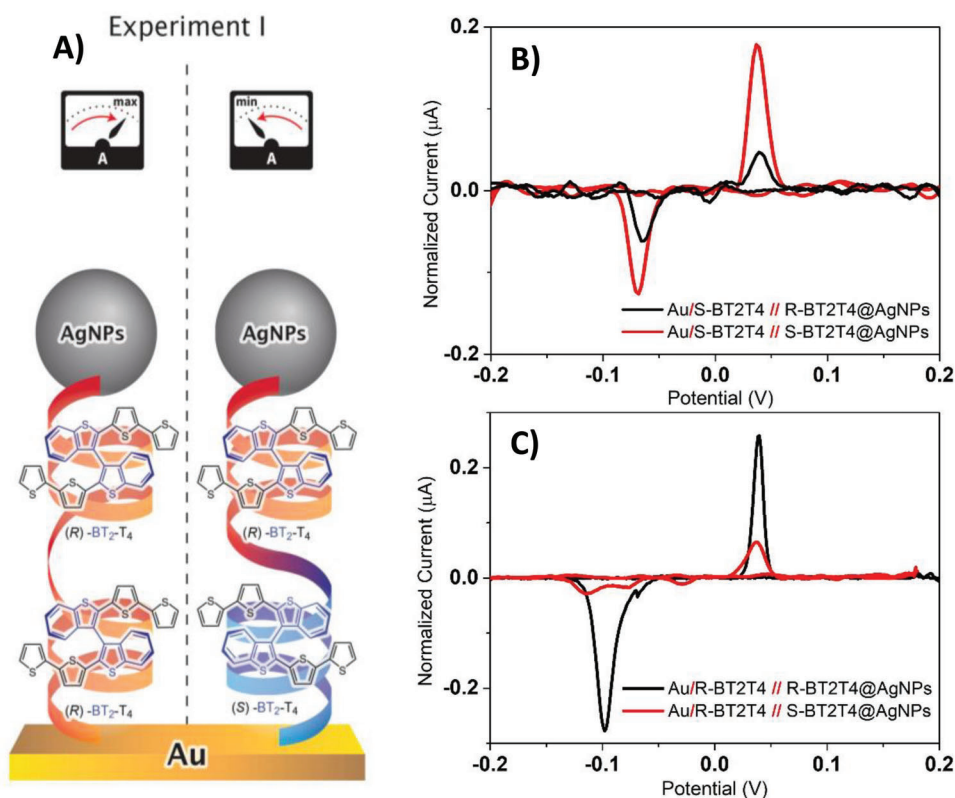


**Figure 2.** A) Actual experimental implementation of Experiment I: chiral recognition electrochemistry. Cyclic voltammetry (CVs) are recorded for all the possible handedness combinations. B) Black Au|(S)-BT<sub>2</sub>T<sub>4</sub>|(R)-BT<sub>2</sub>T<sub>4</sub>@AgNP and red Au|(S)-BT<sub>2</sub>T<sub>4</sub>|(S)-BT<sub>2</sub>T<sub>4</sub>@AgNP. C) Black Au|(R)-BT<sub>2</sub>T<sub>4</sub>|(R)-BT<sub>2</sub>T<sub>4</sub>@AgNP and red Au|(R)-BT<sub>2</sub>T<sub>4</sub>|(S)-BT<sub>2</sub>T<sub>4</sub>@AgNP. An amount of 0.1 M KCl in aqueous solution is the base electrolyte.

direction: spin-injection occurs via the ferromagnetic Ni tip. In Figure 4B, (R)-BT<sub>2</sub>T<sub>4</sub> adsorbed on gold (Au|(R)-BT<sub>2</sub>T<sub>4</sub> interface), the largest current is found for the magnet UP orientation, while in Figure 4C the opposite is found: for the (S)-BT<sub>2</sub>T<sub>4</sub> enantiomer adsorbed on gold (Au|(S)-BT<sub>2</sub>T<sub>4</sub> interface).

The quantitative analysis of mc-AFM *I*-*V* curves as a function of magnet orientation, Figure 4B,C allows to determine a maximum spin-polarization value, which is found ranging between 28% to 30%, obtained for a ±2 V bias.

## 2.2. Hybrid Interfaces Characterization

### 2.2.1. XPS S 2p Results

The *I*-*V* curves accuracy relies on the accurate fabrication of complex hybrid multilayered molecular architectures, a crucial task. A substantial effort was devoted to the in depth characterization of the interfaces, by cross-checking results obtained by using independent surface sensitive techniques: XPS, Raman, and electrodesorption. The XPS experimental outcome was also compared with theoretical results. In particular, **Figure 5** shows XPS S 2p XPS spectra recorded for the interfaces used in the Experiments I, II, and III. Figure 5a sets out S 2p spectra of the BT<sub>2</sub>T<sub>4</sub>@AgNPs interface, the peak found in the 168 to 158 eV range is due to three different components: sulfur involved in a strong chemical interaction at 161.4 eV, free not-bound thio-

phene sulfur at 163.6 eV, and oxidized sulfur at 166 eV, these components are indicated in Figure 5a as S<sub>bound</sub>, S<sub>thioph</sub>, and S<sub>ox</sub>, respectively. The prominent S 2p 161.4 eV component stems from the strong S-Ag interaction (bound sulfur) giving due reason to the effective AgNPs capping. Figure S3 (Supporting Information) shows the BT<sub>2</sub>T<sub>4</sub>@AgNPs XPS survey, C 1s and Ag 3d spectra, together with the relevant Voigt doublets components fitting (compare the Supporting Information for details concerning the fitting procedure). Figure 5b shows XPS S 2p spectra for the Au|BT<sub>2</sub>T<sub>4</sub> interface, the peak in the 170 to 158 eV region can be effectively fitted by two components centered at 163.6 (due to the free, not-chemically-bound thiophene) and 161.4 eV (associated to the S atoms of the BT<sub>2</sub>T<sub>4</sub> adsorbed to the Au surface<sup>[45–49]</sup>). The absence of any signal for energy values larger than 166.5 eV further supports the effective gold surface functionalization (signals at energies larger than 166.5 eV are typical of oxidized sulphur).<sup>[50,51]</sup> The component relevant to chemisorbed sulphur appears more intense than the free thiophene one, this suggests a disposition of the BT<sub>2</sub>T<sub>4</sub> which maximizes the number of sulphur atoms interacting with the gold surface.<sup>[52–54]</sup> The inset in Figure 5b sets out the S 2p core level spectrum using a 260 eV probing photon energy (Elettra synchrotron facility, 0.1 eV of resolution). Figure 5b inset analysis allows to appreciate a neat separation between the two components of the doublet, the relative intensity of the two main components at 163.6 and 161.4 eV is reversed, with respect to Figure 5b main spectrum, taken at 1253.6 V of photon energy. Remarkably, a lower energy of the

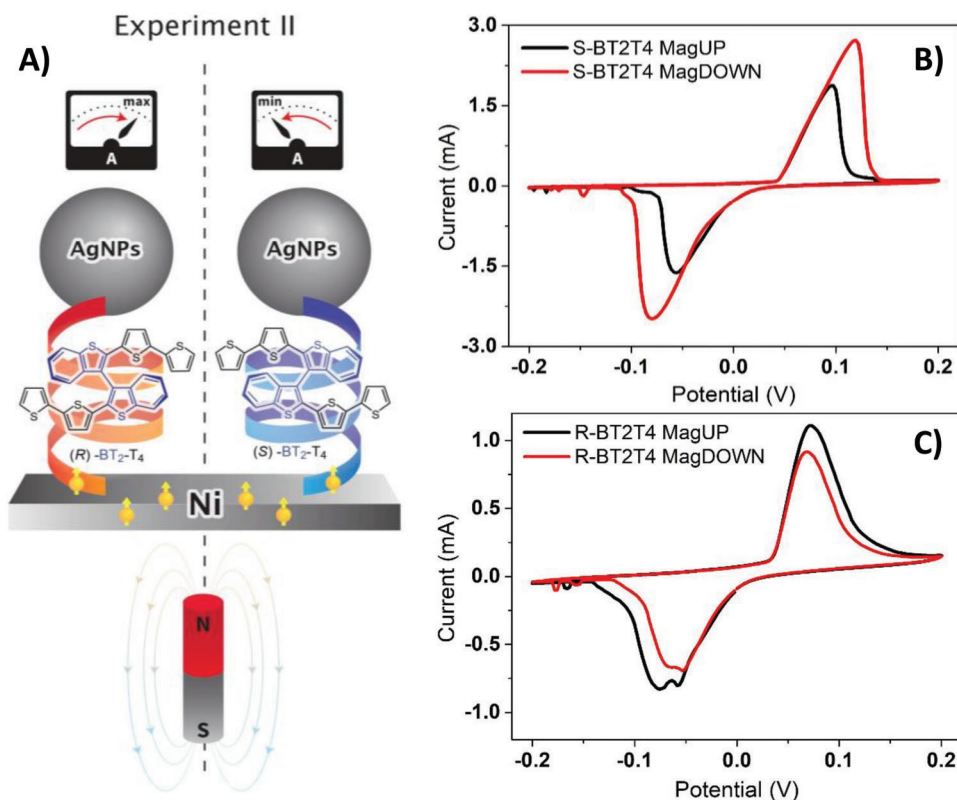


**Figure 3.** Experiment II: spin-dependent cyclic voltammetry (CVs). A) Schematic representation of Experiment II setup B) Ni|(S)-BT<sub>2</sub>T<sub>4</sub>@AgNPs: black line MagUP, red curve MagDOWN. C) Ni|(R)-BT<sub>2</sub>T<sub>4</sub>@AgNPs: black line MagUP, red curve MagDOWN.

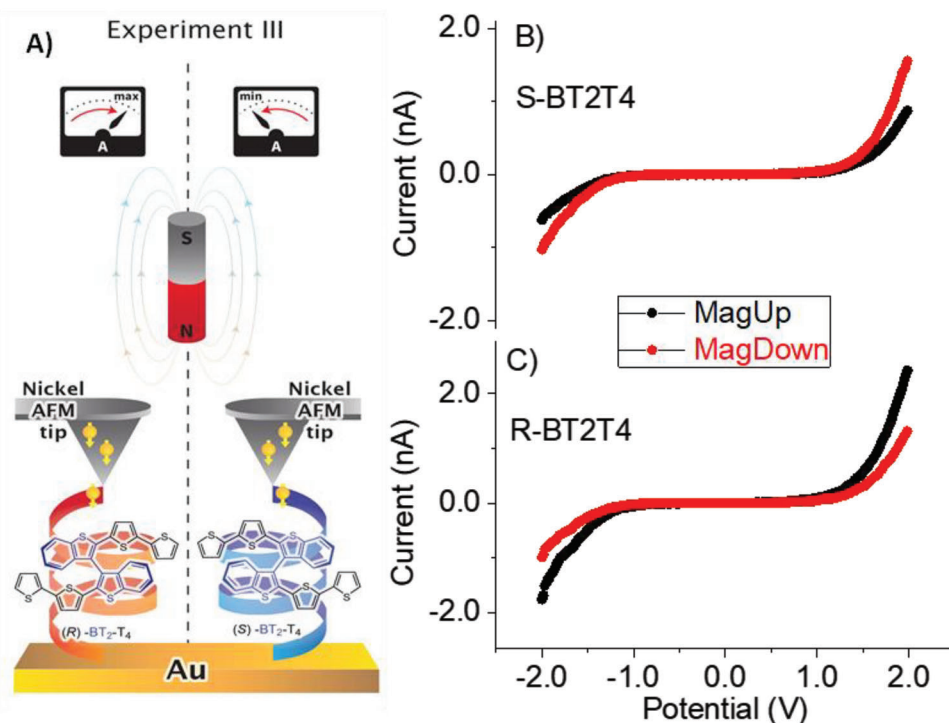


**Figure 4.** A) Schematic representation of Experiment III setup: magnetic conductive probe atomic force microscopy (mc-AFM). Au substrate and Ni ferromagnetic tip: black line MagUP orientation, red line MagDOWN orientation. B) Au|(S)-BT<sub>2</sub>T<sub>4</sub> interface. C) Au|(S)-BT<sub>2</sub>T<sub>4</sub> interface. Circle dimension in *I*-*V* curves is representative of a  $\pm 0.1$  nA sensitivity, corresponding to a 5% standard deviation on the largest current value. See Section S5 and Figure S15 (Supporting Information), for more details concerning *I*-*V* experimental data acquisition and data sensitivity.

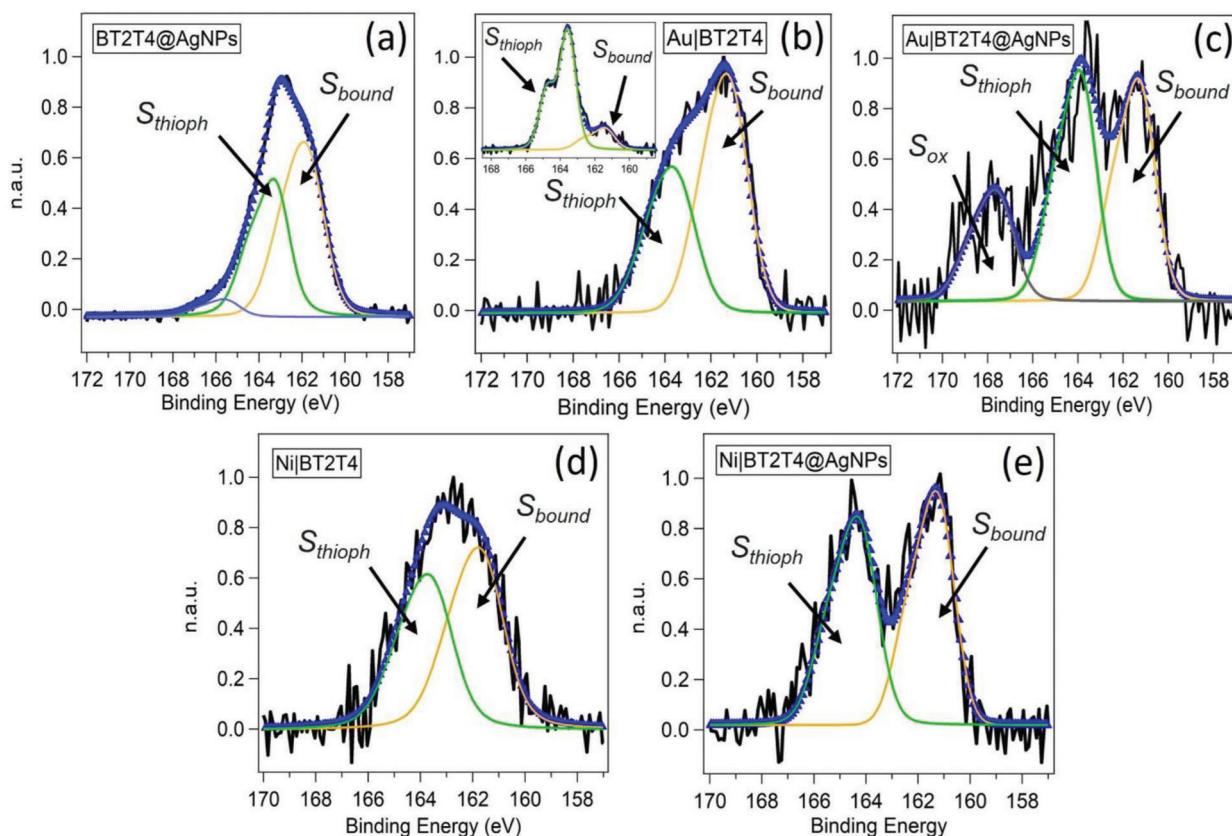


**Figure 5.** S 2p X-ray photoemission spectroscopy (XPS) spectra. A)  $\text{BT}_2\text{T}_4$ @AgNPs capped nanoparticles. B) Au| $\text{BT}_2\text{T}_4$  interface. C) Au| $\text{BT}_2\text{T}_4$ @AgNPs interface. D) Ni| $\text{BT}_2\text{T}_4$  interface. E) Ni| $\text{BT}_2\text{T}_4$ @AgNPs interface. Ni| $\text{BT}_2\text{T}_4$ @AgNPs interface. The black curve represents the experimental spectra, the thick blue line curve are the overall fitted data. Individual components: thin orange line is the bound sulfur, thin green line the unbound sulfur, thin sky-blue line the oxidized sulfur.

probing photon implies a higher surface sensitivity, this allows for a more sensitive detection of electrons ejected from sulfur atoms dangling toward the vacuum, i.e., far (not-bonded) from the gold surface. All in all, both high- and low-energy XPS results suggest that a monolayer of  $\text{BT}_2\text{T}_4$  is chemisorbed on gold maximizing the interactions between sulfur and gold. A picture which is consistent also with theoretical results relating to the optimization of the  $\text{BT}_2\text{T}_4$  on a gold slab (as described in detail in the Supporting Information). Figure 5c shows XPS S 2p spectra for the Au| $\text{BT}_2\text{T}_4$ @AgNPs, note that the spectrum is rather noisy, but this result is consistent with sulfur of thiophene buried in between the gold and silver. The two components at 161.4 (orange solid curve) and 163.9 eV (green solid curve) are attributed to bound ( $S_{\text{bound}}$ ) and free ( $S_{\text{thioph}}$ ) sulfur atoms, respectively, their difference in energy, 1.5 eV, is consistent with results present in the literature.<sup>[55]</sup> The component at 168.1 (black solid curve) eV is assigned to oxidized sulfur.<sup>[55]</sup> Figure 5d,e shows XPS S 2p spectra for the Ni| $\text{BT}_2\text{T}_4$  and Ni| $\text{BT}_2\text{T}_4$ @AgNPs interfaces, respectively. Spectrum in Figure 5d features a well-defined peak, which has the typical line-shape of thiols and thiophene-based SAMs: in fact, both the 161.4 eV (free S atoms) and the 163.6 eV (bound S atoms) are present, indicated as  $S_{\text{thioph}}$  and  $S_{\text{bound}}$ , respectively (in agreement with the results of Figure 5b). No components of energy larger than 166.5 eV are present, indicating

a negligible amount of oxidized sulfur. Ni| $\text{BT}_2\text{T}_4$ @AgNPs interface, Figure 5e: the S 2p spectrum analysis shows a very close agreement between Au-based and Ni-based systems. Also the pattern of the spectrum is noisier with respect to the Ni| $\text{BT}_2\text{T}_4$  interface (Figure 5d), again in tight agreement with the results obtained on gold.

### 2.2.2. Electrodesorption

**Electrodesorption: Au| $\text{BT}_2\text{T}_4$  Interface:** Figure 6 sets out CV curves of a ferrocyanide  $5 \times 10^{-3}$  M, ferricyanide  $5 \times 10^{-3}$  M (Fe(III)|Fe(II) redox couple) KCl 0.1 M aqueous solution, the Au| $\text{BT}_2\text{T}_4$  interface serves as the WE. The red curve in Figure 6a shows the CV recorded using a bare Au surface WE as a reference. A peak-to-peak potential separation of about 70 mV is obtained, and the relevant fitting yields a charge transfer rate constant of  $0.1 \text{ cm s}^{-1}$ . The black curve in Figure 6a shows the CV recorded using a Au| $\text{BT}_2\text{T}_4$  WE, please note a decrease (about 50%) in the redox current peaks, with respect to the bare gold. Moreover, a larger peak-to-peak potential difference, between the forward and backward redox peaks (about 0.350 V) is found, typical of a slower electron transfer kinetics. The relevant curve fitting yields a  $k^0$  charge transfer constant of about  $5 \times 10^{-4} \text{ cm s}^{-1}$ .

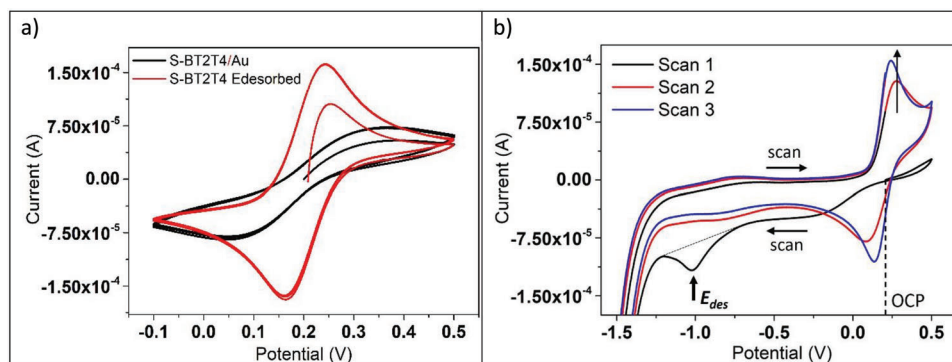
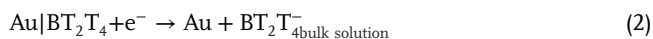


**Figure 6.** Cyclic voltammetry (CV) curves  $5 \times 10^{-3}$  M Fe(III)|Fe(II) redox couple in 0.1 M KCl aqueous solution, recorded at  $0.1 \text{ V s}^{-1}$  potential scan rate. Pt and Ag/AgCl/KCl<sub>sat</sub> are the counter electrode (CE) and reference electrode (RE), respectively. A) Solid black line Au|BT<sub>2</sub>T<sub>4</sub> working electrode (WE). Solid red line CV recorded after the BT<sub>2</sub>T<sub>4</sub> electrodesorption. B) CV curves for the electrodesorption procedure,  $0.5 \text{ V s}^{-1}$  potential scan rate. Solid black line: first CV cycle, starting from OCP to 0.5 V, then the potential is scanned from 0.5 to  $-1.5 \text{ V}$ . Solid red curve is the second scan  $-1.5$  to  $0.5 \text{ V}$  potential range. Solid blue lines: subsequent cycles, carried out in the  $-1.5$  to  $0.5 \text{ V}$  potential range.

Indeed, also the CV measured after the BT<sub>2</sub>T<sub>4</sub> electrodesorption procedure, Figure 6b CVs, is reported in Figure 6a, but it overlaps exactly with the CV obtained for the bare Au surface. A further clear-cut indication of the effective BT<sub>2</sub>T<sub>4</sub> chemisorption on gold.

Such considerations are also supported by a quantitative assessment of electrodesorption CVs. Compare the CV curves reported in Figure 6b: in the anodic part of the first CV scan, from OCP (*i.e.*,  $+0.24 \text{ V}$ ) to  $0.5 \text{ V}$  (black line), much lower currents are observed with respect to the bare Au surface (subsequent scans, as well as comparison with Figure 6a bare Au CV). The cathodic part of the first scan features a broad shoulder at about  $-0.39 \text{ V}$  with a  $-5 \times 10^{-5} \text{ A}$  current (this current value compares well with the backward current recorded on the modified electrode, *i.e.*, the Figure 6a, black curve). Scanning more negative a neat current peak is present in the first scan at  $-1.05 \text{ V}$  (which can be related to BT<sub>2</sub>T<sub>4</sub> electrodesorption), indicated by an arrow ( $E_{\text{des}}$ ) in Figure 6b. The latter peak is absent in the successive CV cycles (red and blue curves). The redox reaction underlying the  $E_{\text{des}}$  current peak can be assumed as follows (3):



Focusing the attention in the potential range between  $-0.1$  and  $0.5 \text{ V}$ , after the first potential scan up to  $-1.5 \text{ V}$  which means after the electrodesorption, the CV becomes coincident to that measured on the bare Au. Thus, the BT<sub>2</sub>T<sub>4</sub> electrodesorption peak potential,  $E_{\text{des}}$  marks the boundary between the functionalized Au|BT<sub>2</sub>T<sub>4</sub> (Figure 6a, black line) and the bare Au behavior (Figure 6a, red line). Taken together, all these results provide a consistent indication that the incubation of gold in the BT<sub>2</sub>T<sub>4</sub> solution yields a functionalized surface by a BT<sub>2</sub>T<sub>4</sub> SAM. Moreover, integration of the peak current at the  $E_{\text{des}}$  potential value (Figure 6b, black curve) allows to estimate the area of BT<sub>2</sub>T<sub>4</sub> adsorbed on the Au surface, which is found to be about  $50 \text{ \AA}^2$ . The latter value is consistent with a surface coverage in the one to two monolayers range, with a BT<sub>2</sub>T<sub>4</sub> disposition allowing for the closest contact between sulfur atoms of the BT<sub>2</sub>T<sub>4</sub> thiophene backbone and the gold surface (please compare the theoretical results Section 6.1, Supporting Information).

**Electrodesorption: Ni|BT<sub>2</sub>T<sub>4</sub> Interface:** Figure 7 displays CV measurements concerning the BT<sub>2</sub>T<sub>4</sub> electrodesorption: Ni|BT<sub>2</sub>T<sub>4</sub> interface. CVs were recorded before (Figure 7a, black curve) and after the electrodesorption experiment (Figure 7b, red curve),  $5 \times 10^{-3}$  M Fe(III)|Fe(II) in 0.1 M KCl aqueous solution. Figure 7b shows the BT<sub>2</sub>T<sub>4</sub> electrodesorption experiment CVs. The BT<sub>2</sub>T<sub>4</sub> electrodesorption underlies the current peak,  $E_{\text{des}}$ , in the solid red curve Figure 7b. On the whole the electrodesorption experiment yields results in tight comparison with the electrodesorption experiment carried out in the case of the Au substrate. The peak-to-peak potential difference decreases after BT<sub>2</sub>T<sub>4</sub> electrodesorption: compare black and red CV curves in Figure 7b.

### 3. Conclusions

This work relies upon the idea to exploit the charge transmission process (which is made quantitative recording  $I-V$  curves) to gain quantitative insight on the conductive/blocking properties of chiral interfaces. The results can be summarized in three different achievements.

1) Current peak maxima of the  $I-V$  curves in Exp I are found to depend on the symmetric and dissymmetric nature of the chiral interface, in a classical chiral-recognition electrochemical experimental arrangement. Where the handedness of the electrode surface is probed exploiting a chiral redox couple.<sup>[8]</sup> In our case handedness is imparted by exploiting enantiomers of the same chiral compound, thus differences in the  $I-V$  curves are only due to chiral-recognition as the chemical nature of the molecules is the same. Remarkably,  $I-V$  curves in Exp II and III are found to be spin-injection dependent. As a consequence, the difference in current of  $I-V$  curves controlled by chiral-recognition can be explained on the basis of the CISS effect: handedness S is conducting the UP spin, which yields “high” conduction if the subsequent facing layer handedness is S (symmetric interface), but yields “low” if conduction of the subsequent facing layer handedness is R (dissymmetric interface), swapping S and R handedness yields exactly the mirror-opposite situation. This explanation is inferred by the ability of spin-injection to yield  $I-V$  curves (SDE and mc-AFM experiments) whose charge

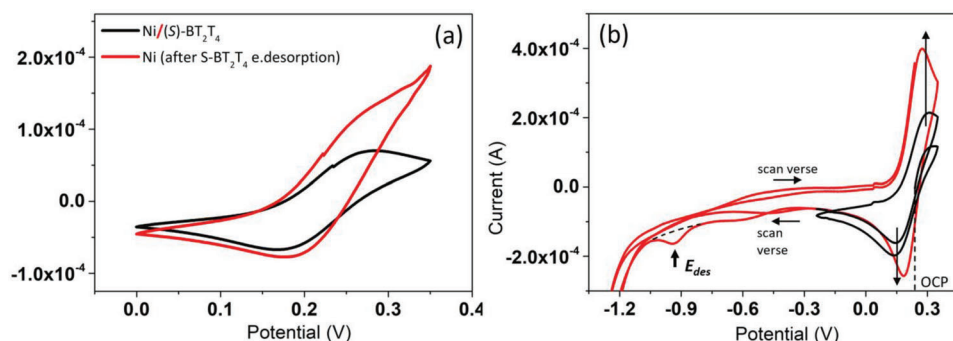


**Figure 7.** Cyclic voltammetry (CV) curves  $5 \times 10^{-3}$  M Fe(III)/Fe(II) redox couple in 0.1 M KCl aqueous solution. Pt and Ag/AgCl/KCl<sub>sat</sub> are the counter electrode (CE) and reference electrode (RE), respectively. A) Solid black line Ni|BT<sub>2</sub>T<sub>4</sub> WE. Solid red line CV recorded after the BT<sub>2</sub>T<sub>4</sub> electrodesorption, 0.1 V s<sup>-1</sup> is the potential scan rate. B) CV curves for the electrodesorption procedure, 0.5 V s<sup>-1</sup> potential scan rate. Solid black line: first CV forward cycle, starting from OCP to 0.5 V, then the potential is scanned from 0.5 and reversed at -0.2 V. Solid red lines: subsequent cycles, carried out in the -1.5 to 0.5 V potential range. Upward and downward arrows indicate the CV oxidation and reduction peaks before the electrodesorption.

transmission efficiency depends on the interface handedness. We can conclude that spin is a hidden driving force in chiral recognition. Indeed, the paradigm of chiral-recognition as a spin-driven process falls in line with experimental results observed in the case of ultrahigh vacuum experiments of polarized-electrons scattering with chiral molecules<sup>[26,27,56]</sup> and the so-called chiral-induced spin selectivity (CISS) effect.<sup>[25]</sup> Furthermore, the spin-based chiral recognition model here proposed fits theoretical results showing the crucial role of SOC in the charge transmission of chiral molecular architectures, as proposed by Cuniberti, Herrmann, and Mujica.<sup>[30,39–41,57]</sup>

2) Furthermore, chemisorption of the thiophene based BT<sub>2</sub>T<sub>4</sub> on Au, Ni, and Ag allows to prepare (tunable) robust and reproducible chiralized interfaces, via facile wet chemistry preparation. Thus chiral thiophene based oligomers appear a promising class of compounds to be exploited in organic electronics and spintronics (a SP% of about 30% is found in mc-AFM measurements) applications.

3) Chiral-capped AgNPs have been used as reversible redox probe, proving to be of facile preparation and robust electrochemical behavior. The properties of chiral-capped AgNPs can be easily tuned by selection of suitable chiral oligothiophenes. Moreover, the standard reversible potential is much more negative (about 0 V with respect to Ag/AgCl/KCl reference electrode) compared to both the Fe(III)/Fe(II) and ferrocene based chiral organics redox couples (about 0.24 V). This makes chiral-capped AgNPs well suited to be exploited in the case of electrodes which can be easily oxidized.

## 4. Experimental Section

**Chemicals:** Merck ethanol solvent  $\geq 99.5\%$ , Sigma–Aldrich Sodium Nitrate NaNO<sub>3</sub>  $\geq 99.0\%$ , Sigma–Aldrich potassium sulfate K<sub>2</sub>SO<sub>4</sub>  $\geq 99.0\%$ , Sigma–Aldrich potassium chloride KCl, Sigma–Aldrich ferrocyanide K<sub>4</sub>[Fe(CN)<sub>6</sub>], and Sigma–Aldrich ferricyanide K<sub>3</sub>[Fe(CN)<sub>6</sub>] were used without further manipulation. A ferrocyanide  $5 \times 10^{-3}$  M, ferricyanide  $5 \times 10^{-3}$  M in a KCl 0.1 M aqueous solution was referred as Fe(III)/Fe(II) redox couple in the text. BT<sub>2</sub>T<sub>4</sub> was synthesized as described in Sannicolò et al.<sup>[58]</sup>

**Gold Functionalization:** Quasi-Au(111) surfaces were obtained by e-beam evaporation of 100 nm of gold, on a silicon substrate (Siltronix), with

thermally grown 300 nm SiO<sub>2</sub> (100),  $>400 \Omega \text{ cm}^{-2}$ , on an 8-nm-thick Ti adhesion layer, followed by gentle flame annealing just prior to use (in the following Au stays for quasi-Au(111)). Gold functionalization was obtained by 24 h incubation of the Au surface in a  $5 \times 10^{-3}$  M BT<sub>2</sub>T<sub>4</sub> solution in ethanol.<sup>[59]</sup>

**Silver Nanoparticles Preparation:** Silver nanoparticles (AgNPs) were obtained exploiting the electrochemically based method of Starowicz et al.<sup>[60]</sup> which was successfully used in the production of hybrid thiophene based architectures, obtaining AgNPs ranging between 20 and 50 nm.<sup>[61]</sup>

**Hybrid Chiral Interface Two-Steps Preparation (Au|BT<sub>2</sub>T<sub>4</sub>|AgNPs):** The Au|BT<sub>2</sub>T<sub>4</sub> interface, obtained following the suitable gold functionalization (compare Section S4.2, Supporting Information), was furtherly incubated for 24 h in the AgNPs suspension. In this way, multilayered interfaces were produced with the thiophene derivative acting as a “molecular-thread” between gold and silver (Au|BT<sub>2</sub>T<sub>4</sub>|AgNPs interface).

**BT<sub>2</sub>T<sub>4</sub> Capped AgNPs Preparation BT<sub>2</sub>T<sub>4</sub>@AgNPs:** The electrochemically fabricated AgNPs (vide supra, Section 4.3, Supporting Information) were added to a  $5 \times 10^{-3}$  M BT<sub>2</sub>T<sub>4</sub> ethanolic solution in order to obtain thiophene capped-AgNPs (BT<sub>2</sub>T<sub>4</sub>@AgNPs). The resulting solution was left at rest under dark for 24 h at room temperature.

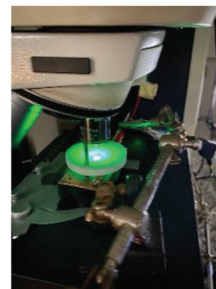
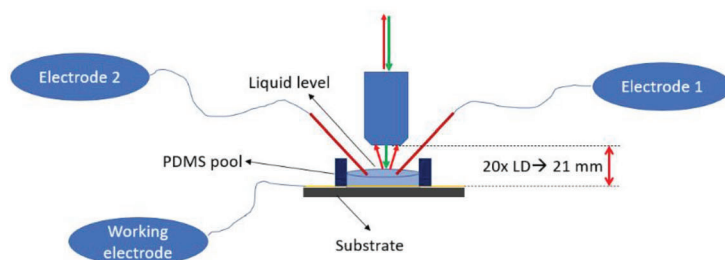
**Hybrid Chiral Interface One-Step Preparation (Au|BT<sub>2</sub>T<sub>4</sub>@AgNPs):** Au surfaces were incubated within the capped AgNPs (BT<sub>2</sub>T<sub>4</sub>@AgNPs) suspension (compare previous Section S4.5, Supporting Information) for 24 h in the dark at room temperature. This procedure allows for a one-step preparation of the Au|BT<sub>2</sub>T<sub>4</sub>@AgNPs hybrid interface.

**Nickel Functionalization:** Ni surfaces were obtained by e-beam evaporation of 100 nm of nickel, on a silicon substrate (Siltronix) with thermally grown 300 nm SiO<sub>2</sub> (100),  $>400 \Omega \text{ cm}^{-2}$ , on an 8-nm-thick Ti adhesion layer. A one-step Ni functionalized preparation strategy was followed.<sup>[62]</sup> Ni functionalized surfaces were obtained by immersion in a BT<sub>2</sub>T<sub>4</sub> solution in ethanol (yielding a hybrid Ni|BT<sub>2</sub>T<sub>4</sub> chiral interface) or a suspension of BT<sub>2</sub>T<sub>4</sub> capped Ag nanoparticles (yielding a hybrid Ni|BT<sub>2</sub>T<sub>4</sub>@AgNPs chiral interface). During the functionalization process the Ni surface was kept at a negative (reducing) potential of -0.3 V, to avoid nickel oxidation.<sup>[62]</sup>

**Electrochemical Setup:** CVs, as well as screening electrochemical measurements not reported, were performed by using an Autolab PGSTAT 128N or CH-Instruments CHI660A potentiostats. A typical three-electrode electrochemical cell was employed. A Pt sheet and a silver chloride reference electrode (Ag/AgCl/KCl<sub>sat</sub>) electrodes were the counter (CE) and reference electrodes (RE), respectively. An amount of 0.1 M KCl and K<sub>2</sub>SO<sub>4</sub> aqueous solutions were used as base electrolytes. As WE different chiral interfaces were used (vide supra the section relevant to the Au and Ni functionalization and AgNPs synthesis). All the potentials reported in this work were referred to the Ag/AgCl/KCl<sub>sat</sub> reference electrode.

**SDE Electrochemical Setup:** All the CVs, and spin-dependent electrochemical measurements in particular, were carried out using a “flat cell”:





**Scheme 1.** Raman spectro-electrochemistry “in situ” setup.

the cell was obtained via lathe-turning of a Teflon rod: for a total cell volume of 3 mL, with a bottom hole of 0.6 cm. The WE was placed at the bottom (typically a shred of about 2 cm length, 1.5 cm width, and 0.5 mm thick. The WE was 200 nm thick metal, Au or Ni, supported on 0.5 mm thick Si wafer), a silicon o-ring of 0.7 cm diameter was placed between the bottom cell hole and WE, avoiding any solution leakage. The permanent magnet was a NdFeB B88 × 0 Grade N42 K&J Magnet, Inc., with a nickel coating: magnetic field at the surface was larger than 0.6 T (6353 Gauss).<sup>[63]</sup> All mechanical parts, WE plate support, nuts, bolts, and rods were made in brass. An exploded view of the cell can be found as the last section in the Supporting Information (Figure S19, Supporting Information).

**UHV Surface Characterization:** XPS measurements were performed using a conventional MgK $\alpha$  source and a hemispherical Omicron EA125 electron analyzer (LFMS lab, Department of Engineering Enzo Ferrari, University of Modena, Italy). Photoemission measurements were performed at normal emission. XPS experimental core-levels spectra have been fitted using Voigt functions (convolution of Gaussian and Lorentzian functions). All measurements were performed at room temperature.

**Raman and Raman In Situ Spectro Electro Chemistry Setup:** Raman spectra were recorded with a Renishaw RM1000 spectrometer coupled to a Leica DLML microscope equipped with 50 $\times$ , 20 $\times$ , and 5 $\times$  objectives. The spectrometer with 250 mm focal length was equipped with a Peltier thermoelectric cooled CCD 1024 × 256 pixels and a diffraction grating 1800 grooves per mm. The Rayleigh scattering was removed with edge filter centered at 514.5 nm allowing for a minimum Raman shift of approximately 100 cm<sup>-1</sup>. The setup allowed for a spatial resolution of about 1  $\mu$ m with the 50 $\times$  objective and a nominal field depth ranging from about 25 to 450  $\mu$ m and a spectral resolution down to 0.5 cm<sup>-1</sup>. The excitation was from an Argon ion gas laser tuned at 514.5 nm with a nominal power of 25 mW. In all the experiments, the power was reduced by neutral density filters to avoid sample damage. In situ measurements were carried out with an in-house Teflon electrochemical cell using the long distance 20 $\times$  objective which guarantee a working distance of 21 mm (**Scheme 1**).

**Magnetic-Conductive Atomic Force Microscopy (mc-AFM):** mc-AFM measurements were performed by using Bruker Scan-analyst AFM. The electrical and magnetic module allows conductive samples to be studied both in contact and peak force TUNA mode. The mc-AFM was used to map the conductivity of films using both a low noise DC technique and a phase locked AC system. By applying electrical bias in the -2 to 2 V range a variation of intensity in the peak force tune mode of AFM, would allow to map conductivity of the sample as a function of the magnetic field direction. In conductive mc-AFM, the sample was electrically biased, and the circuit was completed by providing a connection to ground via the mc-AFM probe chip. Magnetic field (0.1 T) was applied, using Nd-Fe-B permanent magnets, on Ni magnetic tip (Bruker-MESP with spring constant 2.6 N/m) during the measurements. This technique provides insight into the grain structure and allows lateral mapping of the conductivity at the nanoscale. All our scans ( $\approx$ 100) on each point have been obtained at room temperature.

**Calculation Details:** The theoretical data here reported were calculated in the framework of both semiempirical and DFT quantum mechanical based methods, as implemented in the MOPAC suite of programs.<sup>[64]</sup> For the BT<sub>2</sub>T<sub>4</sub> single molecule (neutral and cation species) ab-initio DFT

B3LYP/cc-pVTZ level of theory was used for i) full geometry optimization ii) the calculation of the relevant electronic and vibrational (IR and Raman) spectra. Chemisorption of BT<sub>2</sub>T<sub>4</sub> on both Au and Ni was modelled within the so-called embedded cluster approach. BT<sub>2</sub>T<sub>4</sub> was allowed to relax on top of a (111) surface of a gold or nickel slab, of fixed geometry (corresponding to the experimental crystalline disposition). Both Au(57)|BT<sub>2</sub>T<sub>4</sub> and Ni57|BT<sub>2</sub>T<sub>4</sub> clusters optimization and electronic properties have been calculated by using the PM6 Hamiltonian, as implemented within the MOPAC program.<sup>[64]</sup>

## Supporting Information

Supporting Information is available from the Wiley Online Library or from the author.

## Acknowledgements

CF gratefully thanks financial support from Dipartimento di Ingegneria “Enzo Ferrari” (DIEF), UniMORE, FARD 2021 – linea di azione di tipo 3: “Materiali chirali per batterie al litio e celle a combustibile” and from Consorzio Interuniversitario Nazionale per la Scienza e Tecnologia dei Materiali (INSTM), fondi triennali: “INSTM21MOFONTANESI”. Los Alamos, Center for Integrated Nanotechnologies (CINT), is gratefully acknowledged for measurements performed within Proposal (2022BU0149: CHANT – Chiral cHarge trANsfer co-crysTal). ACJ and SM acknowledge support from Laboratory Directed Research and Development Early Career Award 20220531ECR and 20230854PRD2. Dr. Han Htoon (CINT) is acknowledged for helpful discussion and suggestion. Davide Papazzoni is gratefully acknowledged for the realization of the experiment artistic representations.

## Conflict of Interest

The authors declare no conflict of interest.

## Author Contributions

A.S., S.M., L.P., and T.S. performed experimental measurements and chemicals preparations. M.I. and C.F. performed conceptualization. A.S., L.P., S.M., and A.C.J. performed formal analysis. A.S., S.M., A.C.J., L.P., and T.S. performed investigation. C.F. wrote original draft. P.R.M., T.B., A.S., and L.P. reviewed and edited the work. M.I. and C.F. worked on funding acquisition. All authors have read and agreed to the published version of the manuscript.

## Data Availability Statement

The data that support the findings of this study are available from the corresponding author upon reasonable request.

## Keywords

adsorption, chiral recognition, CISS effect, spin, thiophene

Received: July 31, 2023

Revised: September 9, 2023

Published online: September 29, 2023

- [1] L. D. Barron, *Nat. Mater.* **2008**, *7*, 691.
- [2] J. Stöhr, J. Siegmann, *Magnetism*, Springer Series in Solid-State Sciences, Springer, Berlin **2006**, Vol. 152.
- [3] Y. P. Feng, L. Shen, M. Yang, A. Wang, M. Zeng, Q. Wu, S. Chintalapati, C. R. Chang, *Wiley Interdiscip. Rev.: Comput. Mol. Sci.* **2017**, *7*, e1313.
- [4] H. Lu, J. Wang, C. Xiao, X. Pan, X. Chen, R. Brunecky, J. J. Berry, K. Zhu, M. C. Beard, Z. V. Vardeny, *Sci. Adv.* **2019**, *5*, eaay0571.
- [5] G. L. J. A. Rikken, E. Raupach, *Nature* **2000**, *405*, 932.
- [6] G. Laurent, D. Lacoste, P. Gaspard, *Proc. Natl. Acad. Sci. USA* **2021**, *118*, e20127411118.
- [7] M. Hu, Y. X. Yuan, W. Wang, D. M. Li, H. C. Zhang, B. X. Wu, M. Liu, Y. S. Zheng, *Nat. Commun.* **2020**, *11*, 161.
- [8] S. Fireman-Shoresh, I. Turyan, D. Mandler, D. Avnir, S. Marx, *Langmuir* **2005**, *21*, 7842.
- [9] G. K. E. Scriba, *Chromatographia* **2012**, *75*, 815.
- [10] M. Agnes, A. Nitti, D. A. V. Friend, D. Dondi, D. Merli, D. Pasini, *Chem. Commun.* **2016**, *52*, 11492.
- [11] F. Sannicolò, P. R. Mussini, T. Benincori, R. Martinazzo, S. Arnaboldi, G. Appoloni, M. Panigati, E. Quartapelle Procopio, V. Marino, R. Cirilli, S. Casolo, W. Kutner, K. Noworyta, A. Pietrzyk-Le, Z. Iskierko, K. Bartold, *Chem. - Eur. J.* **2016**, *22*, 10839.
- [12] L. Dong, Y. Zhang, X. Duan, X. Zhu, H. Sun, J. Xu, *Anal. Chem.* **2017**, *89*, 9695.
- [13] T. D. Booth, D. Wahnon, I. W. Wainer, *Chirality* **1997**, *9*, 96.
- [14] V. A. Davankov, *Chirality* **1997**, *9*, 99.
- [15] D. E. Koshland, *Angew. Chem., Int. Ed. Engl.* **1995**, *33*, 2375.
- [16] A. D. Mesecar, D. E. Koshland, *Nature* **2000**, *408*, 668.
- [17] J. L. Greenfield, D. Di Nuzzo, E. W. Evans, S. P. Senanayak, S. Schott, J. T. Deacon, A. Peugeot, W. K. Myers, H. Sirringhaus, R. H. Friend, J. R. Nitschke, *Adv. Mater.* **2021**, *33*, 2100403.
- [18] F. Pop, P. Auban-Senzier, E. Canadell, G. L. J. A. Rikken, N. Avarvari, *Nat. Commun.* **2014**, *5*, 3757.
- [19] Y. Liang, K. Banjac, K. Martin, N. Zigon, S. Lee, N. Vanthuyne, F. A. Garcés-Pineda, J. R. Galán-Mascarós, X. Hu, N. Avarvari, M. Lingenfelder, *Nat. Commun.* **2022**, *13*, 3356.
- [20] C. Wattanakit, Y. B. S. Côme, V. Lapeyre, P. A. Bopp, M. Heim, S. Yadnum, S. Nokbin, C. Warakulwit, J. Limtrakul, A. Kuhn, *Nat. Commun.* **2014**, *5*, ncomms4325.
- [21] X. Han, J. Zhang, J. Huang, X. Wu, D. Yuan, Y. Liu, Y. Cui, *Nat. Commun.* **2018**, *9*, 1294.
- [22] T. van Leeuwen, W. Danowski, E. Otten, S. J. Wezenberg, B. L. Feringa, *J. Org. Chem.* **2017**, *82*, 5027.
- [23] A. Berthod, *Anal. Chem.* **2006**, *78*, 2093.
- [24] A. Kumar, E. Capua, K. Vankayala, C. Fontanesi, R. Naaman, *Angew. Chem., Int. Ed.* **2017**, *56*, 14587.
- [25] K. Ray, S. P. Ananthavel, D. H. Waldeck, R. Naaman, *Science* **1999**, *283*, 814.
- [26] S. Mayer, C. Nolting, J. Kessler, *J. Phys. B: At., Mol. Opt. Phys.* **1996**, *29*, 3497.
- [27] J. M. Dreiling, F. W. Lewis, T. J. Gay, *J. Phys. B: At., Mol. Opt. Phys.* **2018**, *51*, 21LT01.
- [28] S. Mishra, A. Kumar, M. Venkatesan, L. Pigani, L. Pasquali, C. Fontanesi, *Small Methods* **2020**, *4*, 2070038.
- [29] C. Kulkarni, A. K. Mondal, T. K. Das, G. Grinbom, F. Tassinari, M. F. J. Mabesoone, E. W. Meijer, R. Naaman, *Adv. Mater.* **2020**, *32*, 1904965.
- [30] U. Huizi-Rayo, J. Gutierrez, J. M. Seco, V. Mujica, I. Diez-Perez, J. M. Ugalde, A. Tercjak, J. Cepeda, E. San Sebastian, *Nano Lett.* **2020**, *20*, 8476.
- [31] S. Sek, B. Palys, R. Bilewicz, *J. Phys. Chem. B* **2002**, *106*, 5907.
- [32] S. Sek, K. Swiatek, A. Misicka, *J. Phys. Chem. B* **2005**, *109*, 23121.
- [33] A. Paul, R. M. Watson, E. Wierzbinski, K. L. Davis, A. Sha, C. Achim, D. H. Waldeck, *J. Phys. Chem. B* **2010**, *114*, 14140.
- [34] J. D. Slinker, N. B. Muren, S. E. Renfrew, J. K. Barton, *Nat. Chem.* **2011**, *3*, 228.
- [35] I. Carmeli, K. S. Kumar, O. Heifler, C. Carmeli, R. Naaman, *Angew. Chem., Int. Ed.* **2014**, *53*, 8953.
- [36] F. Tassinari, D. R. Jayarathna, N. Kantor-Uriel, K. L. Davis, V. Varade, C. Achim, R. Naaman, *Adv. Mater.* **2018**, *30*, 1706423.
- [37] K. Michaeli, D. N. Beratan, D. H. Waldeck, R. Naaman, *Proc. Natl. Acad. Sci. U. S. A.* **2019**, *116*, 5931.
- [38] M. Innocenti, M. Passaponti, W. Giurlani, A. Giacomino, L. Pasquali, R. Giovannardi, C. Fontanesi, *J. Electroanal. Chem.* **2020**, *856*, 113705.
- [39] V. V. Maslyuk, R. Gutierrez, A. Dianat, V. Mujica, G. Cuniberti, *J. Phys. Chem. Lett.* **2018**, *9*, 5453.
- [40] V. V. Maslyuk, R. Gutierrez, G. Cuniberti, *Phys. Chem. Chem. Phys.* **2017**, *19*, 8848.
- [41] M. S. Zöllner, S. Varela, E. Medina, V. Mujica, C. Herrmann, *J. Chem. Theory Comput.* **2020**, *16*, 2914.
- [42] P. C. Mondal, C. Fontanesi, D. H. Waldeck, R. Naaman, *Acc. Chem. Res.* **2016**, *49*, 2560.
- [43] C. Fontanesi, *Curr. Opin. Electrochem.* **2018**, *7*, 36.
- [44] S. Arnaboldi, M. Magni, P. R. Mussini, *Curr. Opin. Electrochem.* **2018**, *8*, 60.
- [45] F. Terzi, L. Pasquali, M. Montecchi, S. Nannarone, A. Viinikanoja, T. Ääritalo, M. Salomäki, J. Lukkari, B. P. Doyle, R. Seeber, *J. Phys. Chem. C* **2011**, *115*, 17836.
- [46] E. T. Kang, K. G. Neoh, K. L. Tan, *Phys. Rev. B* **1991**, *44*, 10461.
- [47] A. S. Duwez, *J. Electron Spectrosc. Relat. Phenom.* **2004**, *134*, 97.
- [48] L. Pasquali, F. Terzi, M. Montecchi, B. P. Doyle, J. Lukkari, B. Zanfrognini, R. Seeber, S. Nannarone, *J. Electron Spectrosc. Relat. Phenom.* **2009**, *172*, 114.
- [49] C. Vericat, M. E. Vela, G. A. Benitez, J. A. M. Gago, X. Torrelles, R. C. Salvarezza, *J. Phys.: Condens. Matter* **2006**, *18*, R867.
- [50] G. Liu, J. A. Rodriguez, J. Dvorak, J. Hrbek, T. Jirsak, *Surf. Sci.* **2002**, *505*, 295.
- [51] E. Ito, J. Noh, M. Hara, *Surf. Sci.* **2008**, *602*, 3291.
- [52] C. J. Powell, A. Jablonski, *J. Phys. Chem. Ref. Data* **1999**, *28*, 19.
- [53] M. P. Seah, W. A. Dench, *Surf. Interface Anal.* **1979**, *1*, 2.
- [54] A. Jablonski, C. J. Powell, *J. Electron Spectrosc. Relat. Phenom.* **1999**, *100*, 137.
- [55] L. Qie, W. Chen, X. Xiong, C. Hu, F. Zou, P. Hu, Y. Huang, *Adv. Sci.* **2015**, *2*, 1500195.
- [56] A. C. Aragonès, M. Ernesto, F. H. Miriam, G. Nuria, T. Meritxell, J. L. Palma, N. Tao, J. M. Ugalde, G. Ernest, D. P. Ismael, M. Vladimiro, *Small* **2017**, *13*, 1602519.
- [57] M. S. Zöllner, A. Saghatchi, V. Mujica, C. Herrmann, *J. Chem. Theory Comput.* **2020**, *16*, 7357.
- [58] F. Sannicolò, S. Arnaboldi, T. Benincori, V. Bonometti, R. Cirilli, L. Dunsch, W. Kutner, G. Longhi, P. R. Mussini, M. Panigati, M. Pierini, S. Rizzo, *Angew. Chem., Int. Ed.* **2014**, *53*, 2623.
- [59] J. Stöhr, *NEXAFS Spectroscopy*, Springer-Verlag, Berlin Heidelberg **1992**.
- [60] M. Starowicz, B. Stypuła, J. Banaś, *Electrochem. Commun.* **2006**, *8*, 227.
- [61] F. Tassinari, E. Tancini, M. Innocenti, L. Schenetti, C. Fontanesi, *Langmuir* **2012**, *28*, 15505.

- [62] C. Fontanesi, F. Tassinari, F. Parenti, H. Cohen, P. C. Mondal, V. Kiran, A. Giglia, L. Pasquali, R. Naaman, *Langmuir* **2015**, *31*, 3546.
- [63] M. Gazzotti, S. Arnaboldi, S. Grecchi, R. Giovanardi, M. Cannio, L. Pasquali, A. Giacomino, O. Abollino, C. Fontanesi, *Electrochim. Acta* **2018**, *286*, 271.
- [64] J. J. P. Stewart, *MOPAC* **2016**, 2016.